



Contents lists available at ScienceDirect

## International Journal of Fatigue

journal homepage: [www.elsevier.com/locate/ijfatigue](http://www.elsevier.com/locate/ijfatigue)

## Predicting fatigue resistance of nano-twinned materials: Part I – Role of cyclic slip irreversibility and Peierls stress

Piyas B. Chowdhury<sup>a</sup>, Huseyin Sehitoglu<sup>a,\*</sup>, Richard G. Rateick<sup>b</sup>

<sup>a</sup> Department of Mechanical Science and Engineering, University of Illinois at Urbana-Champaign, 1206 W. Green St., Urbana, IL 61801, USA

<sup>b</sup> Honeywell Aerospace, 3520 Westmoor St., South Bend, IN 46628, USA

## ARTICLE INFO

## Article history:

Received 18 December 2013

Received in revised form 16 May 2014

Accepted 22 May 2014

Available online xxx

## Keywords:

Slip irreversibility

Annealing twin

Short crack growth

Microstructure

Fatigue threshold

## ABSTRACT

A combined atomistic and meso-scale model is forwarded to capture the cyclic slip mechanism related to fatigue crack propagation in nano-twinned Ni, Cu and Al. Molecular dynamics simulations have unfolded the importance of cyclic slip–twin interactions and associated slip irreversibilities. Annihilation of cyclic slip, as triggered by forward and reverse plastic flow resistances across a twin boundary, has been found to be the principal cause of irreversibilities. An energetics perspective of relative differences in cyclic flow impedance is provided in terms of generalized stacking fault energies (GSFE). Localized stress concentration of a twin boundary and/or a residual dislocation has been found to modify the intrinsic GSFE levels. A Peierls–Nabarro framework is employed to convert the fault energy consideration into lattice frictional stresses for unobstructed as well as twin-restricted dislocation glide. Mechanistic implications as well as potential use of current findings are discussed in the context of continuum fatigue threshold prediction to be implemented in Part II of this study.

© 2014 Elsevier Ltd. All rights reserved.

### 1. Introduction

Fatigue-induced cracks are the single largest source of service failures in aerospace, naval and ground vehicle components [1]. Advancement of new materials is dependent on developing superior damage tolerance. In that respect, nano-twinned materials hold considerable promise. The extent of literature establishing nanoscale annealing twins as contributors to enhanced monotonic mechanical properties is considerable in the last decade [2–5]. However, their role on fatigue crack growth in particular has not been established until some recent studies reporting an improvement in the damage impedance [6,7]. Resistance to incremental crack advance per cycle of load reversal is decided by the degree of crack-emitted slip irreversibilities as influenced by microstructural obstacles such as twin boundaries. Part I of this study is geared towards establishing pertinent material variables governing twin-induced slip irreversibilities, and developing an understanding of micromechanics of fatigue crack growth in nano-twinned Ni, Cu and Al.

The irreversibility of cyclic slip is strongly dependent on material microstructure, geometry of incident dislocation and interfacial plasticity. As such, we conduct molecular dynamics

simulations to investigate the details of cyclic slip–twin interactions for several fcc metals (Cu, Ni and Al). These analyses facilitate the quantification of associated unstable stacking fault energy,  $\gamma_{us}$ , in particular, subjected to local stress concentrations near a twin boundary and/or a residual dislocation,  $\bar{b}_r$  (created as a consequence of forward slip–boundary intersection). These obstacle-influenced  $\gamma_{us}$  levels are translated into forward and reverse frictional stresses within a Peierls–Nabarro framework. This database of cyclic Peierls stresses for Cu, Ni and Al subsequently serve as necessary input to a continuum fatigue crack growth model (in Part II of the study). The principal purpose of Part I is to develop a physical methodology that can convert these energy barrier considerations into lattice frictional stresses as a prerequisite to predicting twin-affected damage tolerance of these materials (as elaborated in Part II).

Nevertheless, the crucial material parameter,  $\gamma_{us}$  cannot be determined by any experimental measurement technique to-date. Conventionally, density functional theory or molecular statics simulations are widely used to compute  $\gamma_{us}$  by rigidly shearing two atomistic crystal blocks. In the present paper, we utilize molecular dynamics to capture  $\gamma_{us}$  levels during the glide of a dislocation. Such approach is validated by comparing thus-obtained bulk generalized stacking fault energy landscape with that from traditional rigid shear methods. The current method is particularly advantageous over the static rigid shear approach in a unique feature. It

\* Corresponding author. Tel.: +1 217 333 4112; fax: +1 217 244 6534.

E-mail address: [huseyin@illinois.edu](mailto:huseyin@illinois.edu) (H. Sehitoglu).

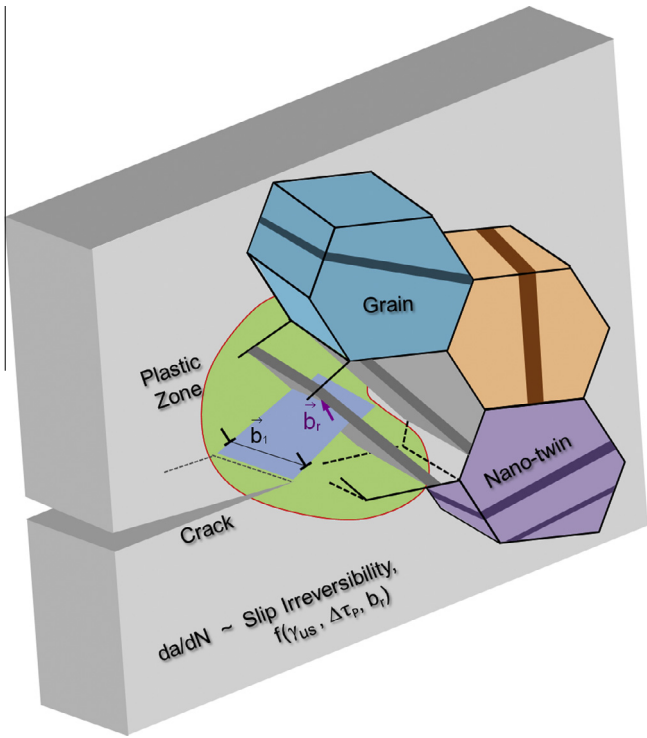


**Fig. 1a.** Schematic illustrating the microstructural environment (characterized by the presence of nano-twins) that an advancing crack would undergo. The crack emits slip ( $\vec{b}_1$ ) within the extent of plastic zone which is on the order of the host grain size. The attendant  $da/dN$  is proportional to the net irreversibility of crack-emitted slip, upon interacting with a twin. The slip irreversibility is a function of unstable stacking fault energy  $\gamma_{us}$ , Peierls stress differential,  $\Delta\tau_p$  and residual dislocation,  $\vec{b}_r$  at the twin boundary.

can model the bulk as well as modified  $\gamma_{us}$  levels for a mobile dislocation under local stresses owing to a twin boundary (during

forward flow) or combined twin boundary and  $\vec{b}_r$  (in reverse flow). Recent advances in Peierls–Nabarro theory allow for the incorporation of the computed  $\gamma_{us}$  levels in extracting corresponding frictional stresses. Following this methodology, the Peierls stresses for bulk lattice friction have been found to be in good agreement with experimental critical resolved shear stresses for Cu, Ni and Al. In light of the aforementioned contemporary knowledge of micro-plasticity, we attempt to develop a physical understanding of discrete dislocation based crack growth mechanism in presence of nano-twins for Ni, Cu and Al.

**Fig. 1a** illustrates a microstructurally short crack progressing in a typical nano-twinned material. The stage I crack advances along the activated slip system, and encounters twins en route. The driving force for the crack growth originates from cyclic slip irreversibilities which is a function of  $\gamma_{us}$ ,  $b_r$  (i.e. the magnitude of  $\vec{b}_r$ ) and Peierls stress differential ( $\Delta\tau_p = \tau_p^{reverse} - \tau_p^{forward}$ ) at the twin boundary. **Fig. 1b** summarizes the general approach of the study: Part I dealing with discrete lattice effects in atomistics and meso-scale, and Part II with continuum level fatigue threshold. In Part I, generalized stacking fault energy (GSFE) curves for unobstructed slip (i.e. free glide) and slip past a coherent twin boundary (CTB) are computed atomistically. The Peierls stress,  $\tau_p$  levels for forward (affected by a CTB) and reverse glide (influenced by both CTB and  $\vec{b}_r = \vec{b}_1 - \vec{b}_2$ ) are extracted from the misfit energy,  $E_{misfit}$  (which is the area underneath a GSFE curve). In Part II, cracks under mode I, II and III loadings are simulated separately using semi-infinite nano-twinned grains in presence of annealing twins with finite spacings ( $d$ ) and lamellar thicknesses ( $t$ ). The non-zero  $\Delta\tau_p$  levels during forward and reverse flow triggers slip irreversibility, and hence the crack advancement.

We have studied three fcc materials (Cu, Ni and Al) with different intrinsic stacking fault energy values. Substantial mechanistic elucidations have been conducted on slip-coherent twin boundary intersection [8–10] in the literature. These studies have established that local stress states and geometrical considerations dictate the outcomes of these reactions. It is possible that a twin may undergo

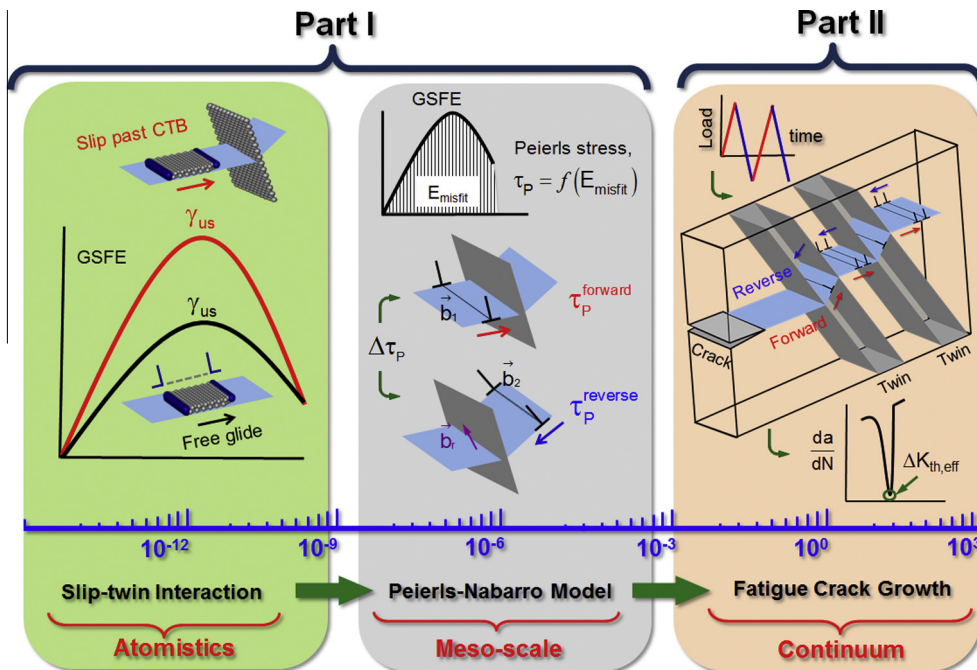


**Fig. 1b.** Schematic elaborating the consideration of associated physics of fatigue crack growth spanning various lengthscales. Atomistics includes the details of molecular dynamics cyclic slip-coherent twin boundary (CTB) interaction, and intrinsic and extrinsic levels of generalized stacking fault energy (GSFE). A Peierls–Nabarro framework utilizes GSFEs as input to compute lattice friction stresses for unobstructed/CTB-induced dislocation glide. Eventually, continuum fatigue crack growth simulations are conducted to assess damage resistance,  $\Delta K_{th,eff}$ .

various local stress states, depending on its relative orientation to the applied loading direction. Thus, two extremities of local stress situations (i.e. maximum and zero resolved shear stresses on twin boundary plane) have been examined in the present analyses. We note that the additional refinement in extracting defect properties from atomistics can still be a subject of further research. Nevertheless, we observe reasonable agreement of damage metrics with earlier experimental findings (in the Part II of this study), utilizing the current atomistic data. The contribution of this report could be deemed as isolating the micro-mechanism of damage propagation, and providing a mechanistic rationale for the effects of twins thereon.

## 2. Methods – molecular dynamics

Molecular dynamics is the simulation of time evolution of atomic nuclei (considered as classical Newtonian particles) by integrating their equations of motions [11]. In the current work, we use LAMMPS (Large-scale Atomic/Molecular Massively Parallel Simulator) simulation package, developed at Sandia National Laboratories ([lammmps.sandia.gov](http://lammmps.sandia.gov)) [12]. Time-dependent effective force field binding the atomic nuclei is modeled through semi-empirical Embedded Atom Model (EAM) formulations [13]. For Cu, Ni and Al, the EAM potentials developed by Mishin et al. [14], Foiles and Hoyt [15] and Mishin et al. [16] have been employed respectively in the present work.

A simulation supercell of a nano-twinned single crystal grain is constructed. Prior to applying deformation, the nano-twinned grain is relaxed using conjugate gradient energy minimization algorithm [11] to obtain a stable configuration. 3-D periodic boundary conditions are enforced to simulate a system of bulk material. A number of supercells have been constructed with different twin thicknesses and source to twin distances. For each system, the size of the supercell is configured to ensure the convergence of physical observables (e.g. temperature, pressure, kinetic and potential energy of the system) to the system size independence. An isobaric-isothermal (also known as NPT) ensemble has been utilized during the deformation i.e. constant  $N$  (total number of atoms),  $P$  (external pressure), and  $T$  (absolute temperature). Nose–Hoover thermostat algorithm is utilized to keep the absolute temperature level at 10 K. Velocity verlet time-integrator has been used to advance the dynamics of applied deformations. Current computational capacity limits molecular dynamics simulations to run for several hundred

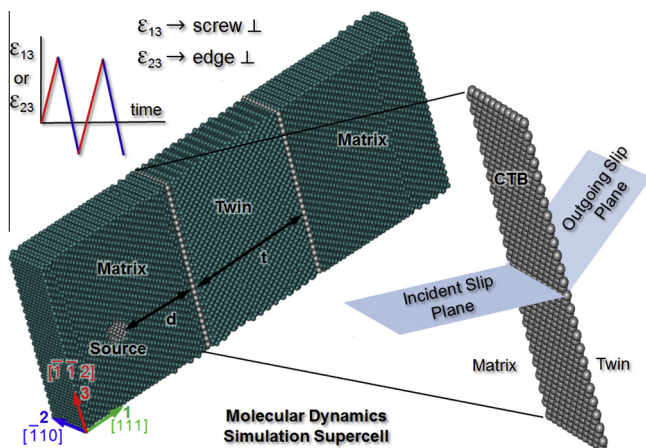
pico-seconds, inevitably leading to high deformation rates. However, the parameters such as glide-induced shear strain, planar fault energies etc. remain unaffected by high strain-rates in our observation. In order to assess the system stress–strain response, the concept of virial stress is utilized, disregarding the kinetic energy contribution in the formulations [17]. To analyze microstructure evolution under applied deformation, atomic configuration viewers, Visual Molecular dynamics [18] (<http://www.ks.uiuc.edu/Research/vmd/>) and AtomEye [19] ([li.mit.edu/Archive/Graphics/A/](http://li.mit.edu/Archive/Graphics/A/)), have been used. For a more detailed description of the simulation procedure adopted in the current work, the readers are referred to Chowdhury et al. [20].

## 3. Results

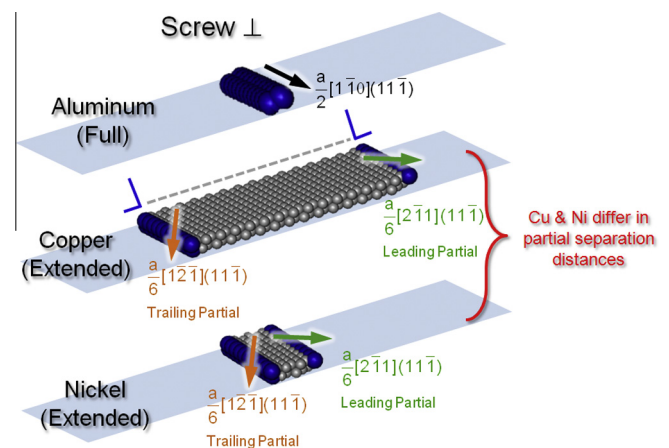
### 3.1. Cyclic slip–twin boundary interaction

Fig. 2a shows a typical molecular dynamics simulation supercell of a nano-twinned single crystal with a dislocation source in the matrix. A cyclic deformation of pure shear (of type  $\epsilon_{13}$  or  $\epsilon_{23}$ ) is applied on the twinned grain, resulting in the nucleation of screw and edge dislocations from the source respectively. The distance from the source to the nearest coherent twin boundary (CTB) is labeled as  $d$ , and the twin thickness as  $t$ . Upon nucleation, dislocations glide on the incident  $(1\ 1\ \bar{1})$  slip plane to intercept the nearest CTB, and transfer inside the twin on the outgoing slip plane of the family  $\{1\ 1\ 1\}$ . The observed dislocation geometries in all three metals are compared in Fig. 2b. In Cu and Ni, the source-emitted dislocations readily emerge as dissociated (i.e. as a pair of leading and trailing Shockley partials of type  $\frac{a}{6}\langle 1\ 1\ 2 \rangle$  connected by a plane of stacking fault). By contrast, Al is found to have  $\frac{a}{2}\langle 1\ 1\ 0 \rangle$  type full dislocations emanating from the source. An extended dislocation in Cu differs from the one in Ni only in terms of the stacking fault width (i.e. the separation distance between the partials).

Table 1 summarizes the results of the slip–twin reactions. The nature of the interaction is a function of local resolved shear stress,  $\tau_{RSS}$  and the geometry of the incident dislocation (i.e. whether it is of edge or screw nature). Under  $\tau_{13}$  shear, the twin boundary plane experiences the maximum  $\tau_{RSS}$  (corresponding to a Schmid factor of 0.5) while  $\tau_{23}$  loading imposes no resolved shear stress (i.e. zero Schmid factor) on the interface. The interactions are summarized in Table 1. A comprehensive detail of cyclic slip–twin reactions is



**Fig. 2a.** Molecular dynamics single crystal structure is suitably oriented with a twin of finite thickness,  $t$  placed at a finite distance,  $d$  away from the dislocation source. Farfield cyclic deformation ( $\epsilon_{13}$  or  $\epsilon_{23}$ ) is applied on the nano-twinned grain, resulting in screw or edge  $\perp$  nucleation respectively from the source. The emitted dislocations glide towards the nearest coherent twin boundary (CTB) on the incident slip plane as dictated by Schmid factor. The incident slip, upon interacting with the CTB, transmits inside the twin on the outgoing slip system.



**Fig. 2b.** Typical dislocation geometries as observed in Al, Cu and Ni crystals in current simulations. In Al, full dislocations of  $\frac{a}{2}\langle 1\ 1\ 0 \rangle$  type are observed while Cu and Ni have extended dislocations (with Shockley partials of  $\frac{a}{6}\langle 1\ 1\ 2 \rangle$  type). The difference between Cu and Ni extended dislocations lies at the separation distance between the leading and trailing partials as shown. In Cu, partials are found to be more widely spaced compared to those in Ni.



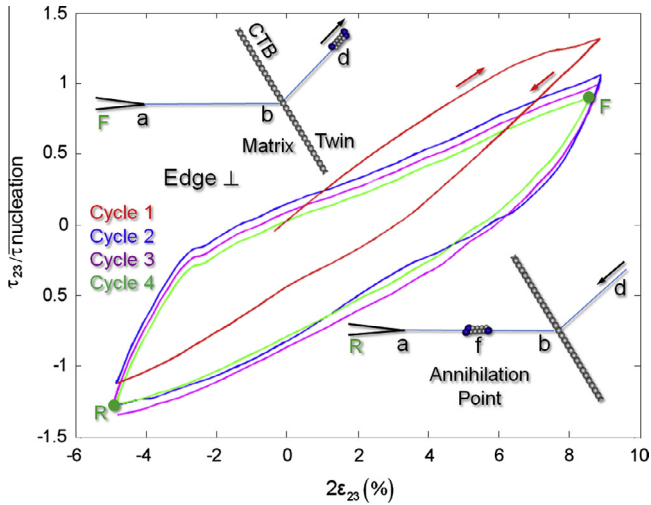


**Fig. 3b.** Quasi-steady state stress–strain response for the edge dislocation case. The inset, corresponding to loading point F, shows the transmitted extended dislocation (inside the twin at d) with a sessile residual Frank partial at point b (not visible). At loading point R, the dislocation from within the twin re-unites with the sessile residual dislocation at b, and re-enters the matrix. The returning dislocation gets annihilated at point f by an oncoming dislocation of opposite sign from the source (at a).

The observed slip irreversibilities are triggered by glide impedances at a twin boundary. In order to estimate the relative resistances to forward and reverse flow past the boundary, we compute standard generalized stacking fault energy plots for Cu, Ni and Al, and study the role of the interface in modifying these energy profiles. We observe a variation in unstable fault energy,  $\gamma_{us}$  (i.e. the maximum fault energy value in these curves) across the matrix–twin interface during forward and reverse flow both for edge and screw dislocations. The current findings are presented in the next section.

### 3.3. Elevation of generalized stacking fault energy at twin boundary

The left hand side schematic in Fig. 5a illustrates a fcc lattice with a cutaway (111) plane and the associated stacking sequence (ABC). The schematic on the right shows the top-view geometry of a (111) plane for dissociation of a full dislocation,  $b_1$  into two partials,  $b_2$  and  $b_3$ . These lattice geometries are used in computing generalized stacking fault energy (GSFE) curves in standard molecular statics and density functional theory simulations. Fig. 5b shows the computed GSFEs for  $\langle 112 \rangle \{111\}$  slip system (considering Burgers vector direction of Shockley partial dislocations) in Ni and Cu, and Al GSFE for  $\langle 110 \rangle \{111\}$  system (i.e. representing to a full dislocation). These GSFE plots are computed in molecular dynamics simulations during the glide of a dislocation.

In the molecular dynamics method, a group of atoms, designated as “tracing atoms” are selected (with an area,  $A = wl$ ) ahead of an oncoming dislocation. The  $w$  and  $l$  values are judiciously selected such that the fault energy to be computed achieves a convergence (which has been found to occur at larger  $l$  and smaller  $w$  values). More detailed discussion regarding the current molecular dynamic approach of computing  $\gamma$  surface could be found in the authors’ previous publication [20]. As the dislocation approaches the tracing atoms, the changing potential energy,  $E$  of the tracing atoms under the influence of the dislocation is compared with the bulk energy,  $E_{bulk}$ .  $E_{bulk}$  corresponds to the potential energy of the tracing atoms when the sweeping dislocation is sufficiently far. Thus, the whole  $\gamma$  surface can be calculated using Eq. (3) as the oncoming dislocation (full or extended) approaches. As an example, when the tracing atoms overlap with the stacking fault

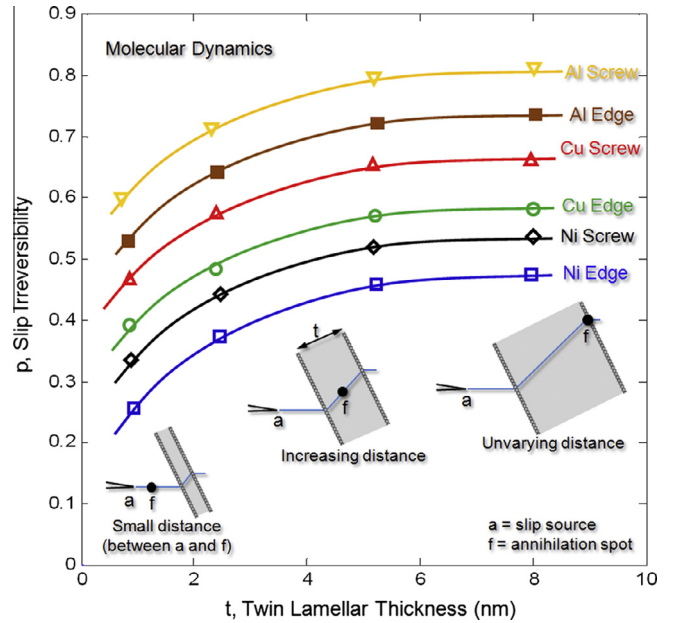


**Fig. 4a.** Molecular dynamics calculation of cyclic slip irreversibilities factor influenced by a nano-twin as a function of the twin lamellar thickness,  $t$ . With gradual increase in  $t$ , the annihilation point  $f$  moves farther away from the source at  $a$ , thereby increasing the irreversible trajectory. However, the  $p$  levels reach a plateau apparently independent of  $t$  which corresponds to a fixed annihilation point due to massive slip activities.

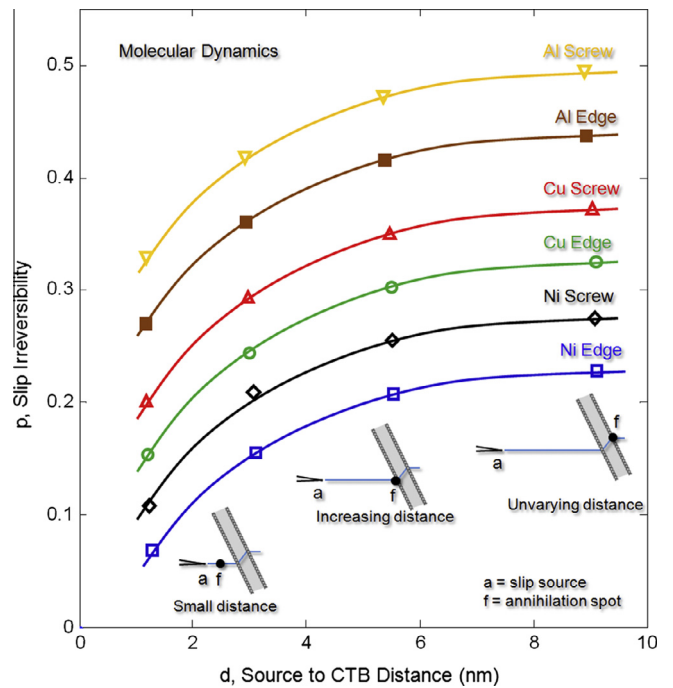


**Fig. 4b.** Slip irreversibilities quantified as a function of source to the nearest coherent twin boundary (CTB) spacing,  $d$ . Similar to  $t$ -dependence, with gradual increase in  $d$ , the annihilation point  $f$  moves farther away from the source at  $a$ , culminating in an increasing irreversible path. The  $p$  values obtain a  $d$ -insensitive saturated stage which corresponds to a fixed annihilation location.

atoms (i.e. once leading partial crosses them), Eq. (3) provides the intrinsic stacking fault energy,  $\gamma_{isf}$  (shown in the inset of Fig. 5b).

$$\gamma = \frac{E - E_{Bulk}}{A} \quad (3)$$

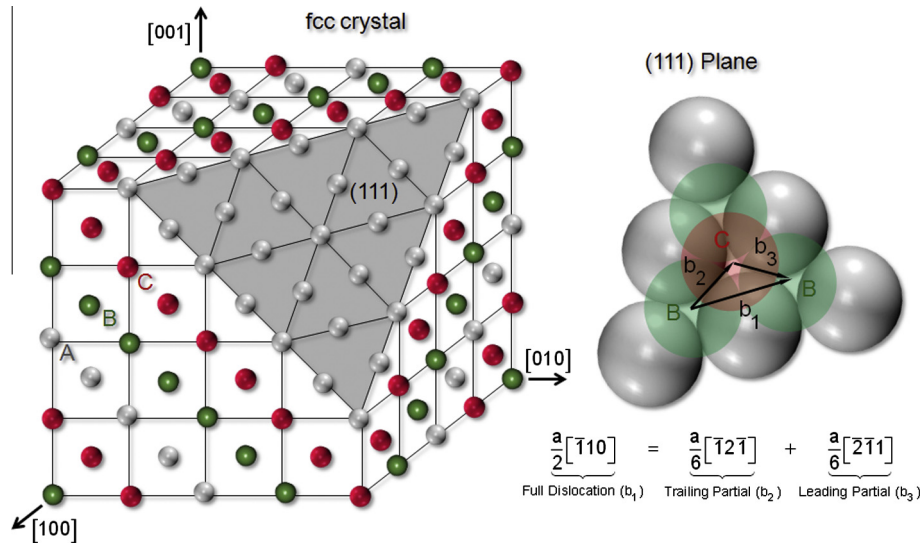


**Fig. 5a.** Left hand side schematic shows an fcc crystal for a pure metal consisting of multiple primitive unit cells with a cut-away section on a (111) plane with the distinct stacking sequence (A – silver atoms, B – green atoms and C – red atoms). Right hand side schematic illustrates the top-view on the (111) plane with three superimposing layers of atoms stacked on top of one another. A full dislocation of  $\frac{a}{2}[110]$  type dislocation dissociates into two Shockley partials of  $\frac{a}{6}[112]$  type. (For interpretation of the references to colour in this figure legend, the reader is referred to the web version of this article.)

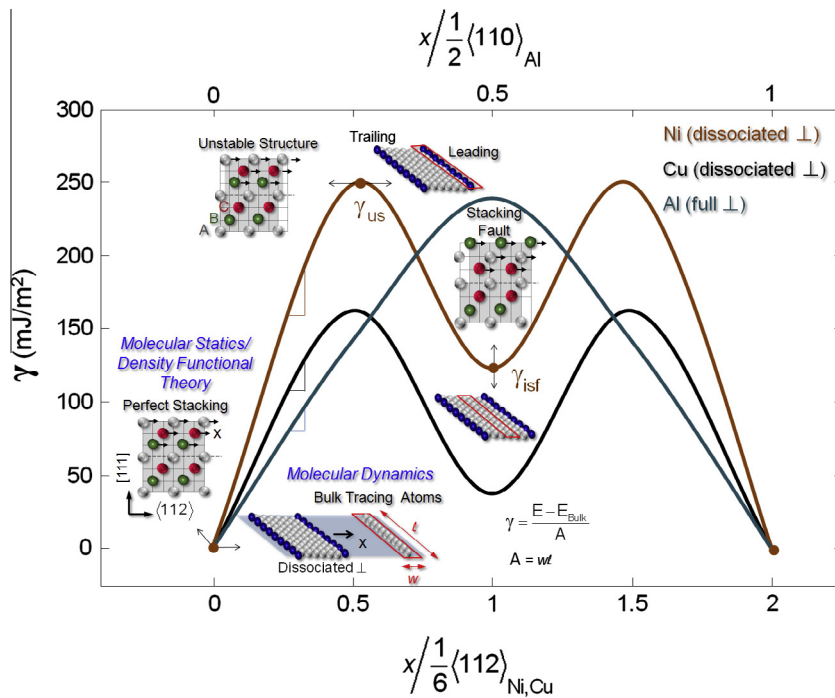


**Fig. 5b.** Generalized stacking fault curves Ni, Cu (along  $\langle 112 \rangle$  slip direction and Al (for  $\langle 110 \rangle$  slip direction) are calculated. By tracing the potential energy differential of a select group of tracing atoms in front of an oncoming glissile dislocation, the corresponding  $\gamma$  values are calculated in molecular dynamics simulations. The selection of tracing atomic area A has been ensured to conform to the convergence of  $\gamma_{us}$  [20]. The atomic stacking configuration shown are only for  $\langle 112 \rangle$  system (i.e. for Cu and Ni only). The peak value in Al curve does not represent the stacking fault energy,  $\gamma_{isf}$  (Al  $\gamma_{isf}$  is listed in Table 2).

Thus-produced GSFE levels, in particular,  $\gamma_{isf}$  and  $\gamma_{us}$  values are in good agreement with those obtained from experiments and density functional theory respectively. It is important to note that in Fig. 5b, Al GSFE for  $\langle 110 \rangle$  system is presented given the fact that no dissociation of slip has been observed during the Al deformation. In order to explain relative slip dissociation propensity, we have additionally computed  $\gamma_{isf}$  and  $\gamma_{us}$  values for Al  $\langle 112 \rangle$  system (not shown in Fig. 5b) in Table 2. The  $\gamma_{isf}$  and  $\gamma_{us}$  data for Al partial system provide a quan-

titative basis to elucidate observed slip geometries in relation to those of Ni and Cu (discussed in details in the Section 4.1). On the other hand, for the purpose of extracting frictional stresses (in Section 3.4), GSFE plots from Fig. 5b for Ni (dissociated), Cu (dissociated) and Al (full) have been considered in their respective Peierls–Nabarro formulations.

The insets in Fig. 5b illustrate the various stages of computing the  $\gamma$  surface by the molecular dynamics method (along with corresponding atomic structures widely used in molecular statics and/

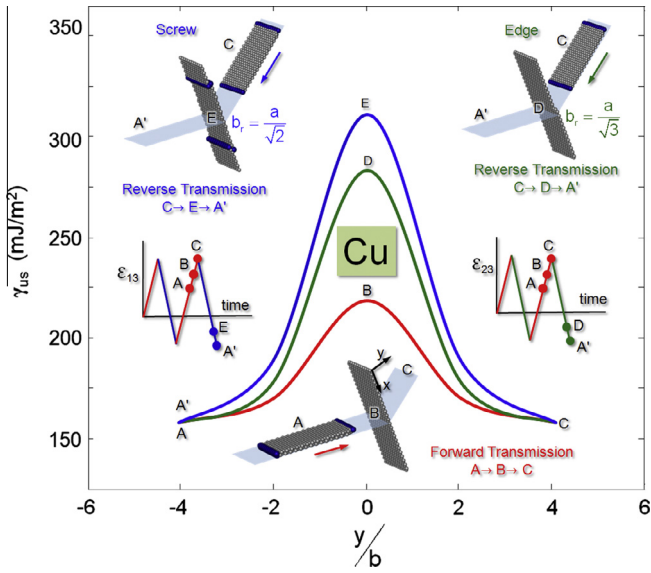


**Fig. 6a.** Unstable stacking fault,  $\gamma_{us}$  levels calculated in Cu for incident screw and edge dislocations for forward and reverse glide past a coherent twin boundary (CTB). The forward-loaded impinging dislocation (either screw or edge) experiences an increasing  $\gamma_{us}$  along  $A \rightarrow B \rightarrow C$  with the peak barrier at point B. On the other hand, returning screw and edge dislocations encounter different energy pathways due to the different magnitudes of the residual Burgers vector ( $b_r$ ) left on the CTB during forward transmission. The greater the magnitude of the  $b_r$  is, the stronger the local stresses are, and hence the higher the peak  $\gamma_{us}$  value becomes. Hence, the screw dislocation (with  $b_r = \frac{a}{\sqrt{2}}$ ) experiences greater barrier compared to the edge (with  $b_r = \frac{a}{\sqrt{3}}$ ). It is important to note that the considerable influences of the local stresses on the bulk  $\gamma_{us}$  levels (at A, A' and C) are very short-ranged, and confined within several Burgers vector from the interface.

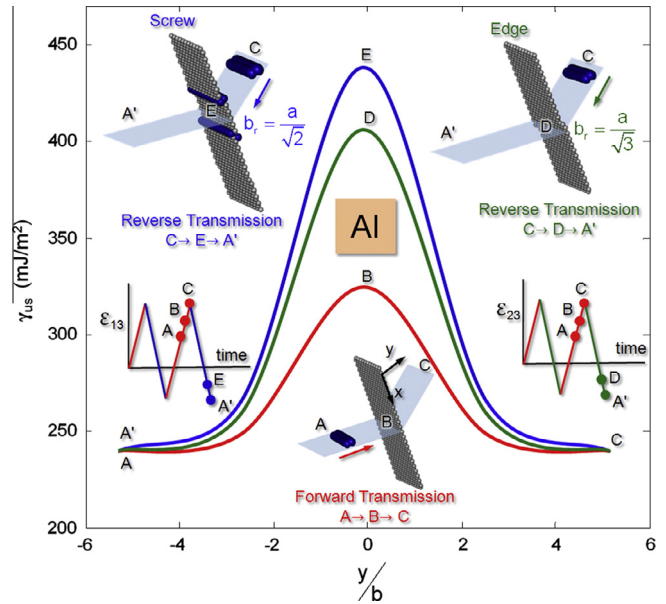


**Fig. 6c.** The  $\gamma_{us}$  energy pathways (in pure Al) for forward and reverse glide past a CTB. Similar to Cu and Ni, the magnitude of  $b_r$  contributes to the existing local stress associated with the CTB (originating from interfacial atomic mismatch), thereby elevating reverse energy pathways ( $C \rightarrow B \rightarrow A'$  and  $C \rightarrow D \rightarrow A'$ ).

or density functional theory methods). The advantage of using the tracing atoms method is that it allows for the GSFE calculation as subjected to local stress concentration (e.g. a twin boundary). As the incident dislocation approaches a twin boundary, it encounters an enhanced degree of resistance to glide, manifested as an elevation from the bulk  $\gamma_{us}$  levels shown in Figs. 6a, 6b and 6c for Cu, Ni

and Al. At an instant of forward loading denoted by A, the approaching edge or screw dislocation (still sufficiently far from the boundary) experiences the bulk  $\gamma_{us}$  level (i.e. unobstructed glide energy barrier). As it gets several Burgers vectors ( $y/b \approx 4-6$ ) near to the interface, the  $\gamma_{us}$  starts increasing, and the maximum level is reached at point B on the interface. The  $\gamma_{us}$  at B represents the maximum energy barrier to forward transmission. For Cu, Ni and Al, these values are calculated to be 227, 340 and 333  $\text{mJ/m}^2$  respectively. As the transmitted dislocation continues its glide away from the twin boundary, it encounters a gradually decreasing level of  $\gamma_{us}$ . The  $\gamma_{us}$  eventually gets down to the bulk level (same as point A) at point C which is located beyond a range of  $4b$  to  $6b$  from the interface. The forward variation in the  $\gamma_{us}$  is shown in red along

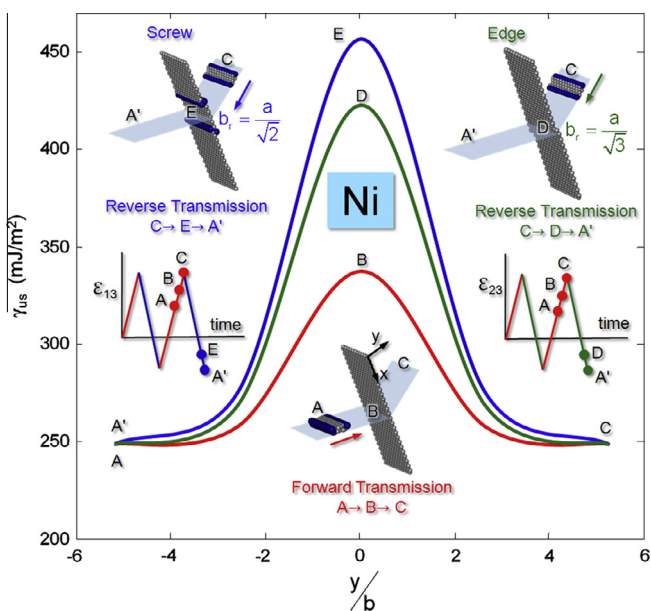


**Fig. 6b.** Variation of  $\gamma_{us}$  (in pure Ni) around a CTB for forward- and reverse-loaded glissile dislocations. The presence of  $b_r$  substantially elevate the reverse energy pathways ( $C \rightarrow B \rightarrow A'$  and  $C \rightarrow D \rightarrow A'$ ) from the CTB-associated stress concentration.

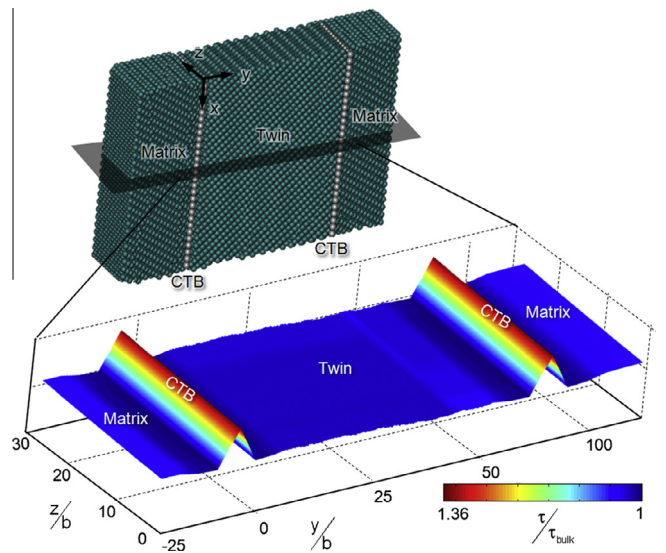


**Fig. 7a.** Molecular dynamics stress concentrations distributed around the coherent twin boundaries (CTB). The local atomic mismatch at the matrix–twin interface generates high local stresses. Any oncoming dislocation would have to overcome such barriers to transmit inside the twin.

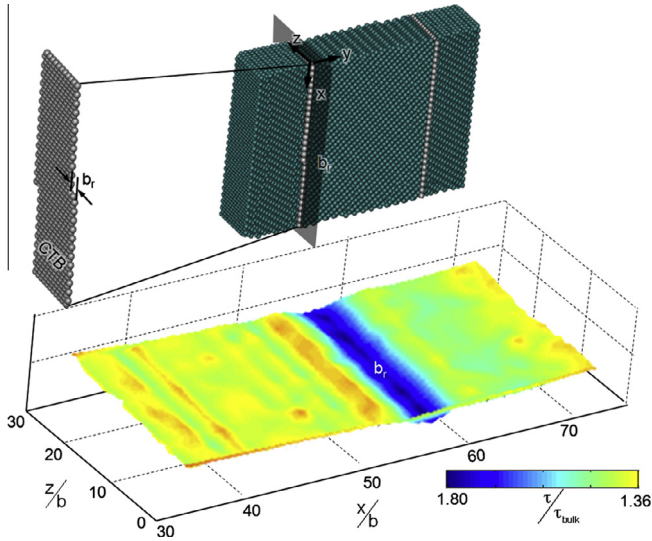


**Fig. 7b.** Stress concentration at the residual Burgers vector ( $b_r$ ) on the CTB. The  $b_r$  shown above is a Frank partial type dislocation ( $\frac{a}{3}[\bar{1}\bar{1}1]$ ) generated during the impingement of an edge dislocation on CTB. The combined stresses associated with both the CTB and  $b_r$  contributes to the enhanced reverse energy barrier for the returning dislocation.

the pathway  $A \rightarrow B \rightarrow C$ . On the other hand, the reverse energy pathways differ for edge and screw dislocations discussed as follows.

During reverse glide, the transmitted dislocation from within the twin has to overcome an enhanced  $\gamma_{us}$  level due to the presence of residual dislocation  $b_r$ . Figs. 6a, 6b and 6c demonstrate that the  $\gamma_{us}$  energy pathways for edge and screw dislocation differ significantly during the reverse glide. In general (both for edge and screw), the maximum energy barrier to be overcome during reverse flow (corresponding to D and E) is always greater than that of the forward one. It has been found that the maximum  $\gamma_{us}$  level at

the interface is proportional to the magnitude of  $\vec{b}_r$ . The screw dislocation (with  $b_r = \frac{a}{\sqrt{2}}$ ) experiences greater resistance compared to the edge dislocation (with  $b_r = \frac{a}{\sqrt{3}}$ ). As seen, the peak magnitude of  $\gamma_{us}$  along  $C \rightarrow D \rightarrow A'$  for an edge dislocation (green curve) is less compared to that of the screw case (blue curve) along  $C \rightarrow E \rightarrow A'$ . For an edge dislocation, the maximum  $\gamma_{us}$  values encountered (at point D) are computed to be 283, 431 and 410  $\text{mJ}/\text{m}^2$  for Cu, Ni and Al respectively. At E (i.e. for screw case), the calculated  $\gamma_{us}$  values for the respective materials are as high as 310, 452 and 441  $\text{mJ}/\text{m}^2$ .

It follows from Figs. 6a, 6b and 6c that the deviation of  $\gamma_{us}$  from the bulk level is confined to a very close proximity to the interface. It has been found that the localized stress field of the twin boundary and/or  $b_r$  extends only on the order of a few Burgers vectors (approximately  $4b$  to  $6b$ ). Such length scale is associated with the range of concentrated stresses around the boundary and/or  $b_r$ . For example, Figs. 7a and 7b illustrates the stress concentration level around the interface and the  $b_r$  for the edge case as calculated from molecular dynamics simulations using virial formulations [13]. In Fig. 7a, the maximum stress in the vicinity of the twin boundary is as high as 1.36 times the bulk stress which gradually subsides beyond  $4b$  (approximately). Fig. 7b shows that the stress concentration of the  $b_r$  is about 1.8 with a similar localized range. These higher stress levels associated with the interface and  $b_r$  underlies the increase of  $\gamma_{us}$  during the flow past a twin boundary. The combined stress contribution of the boundary and  $b_r$  makes the reverse flow more difficult, shown as a relatively greater elevation to  $\gamma_{us}$  as discussed earlier.

The revelation of  $\gamma_{us}$  level discrepancies for forward and reverse transmission provides a rationale for the observed interface-induced slip irreversibilities. The returning dislocation from within the twin experiences a greater resistance which in turn facilitates the nucleation of a dislocation of opposite sign from the source, leading to annihilation of both. In our next step, we employ these  $\gamma$  energies into predicting critical resolved shear stress i.e. Peierls stress ( $\tau_p$ ) both for unobstructed and twin boundary-obstructed glissile motions.

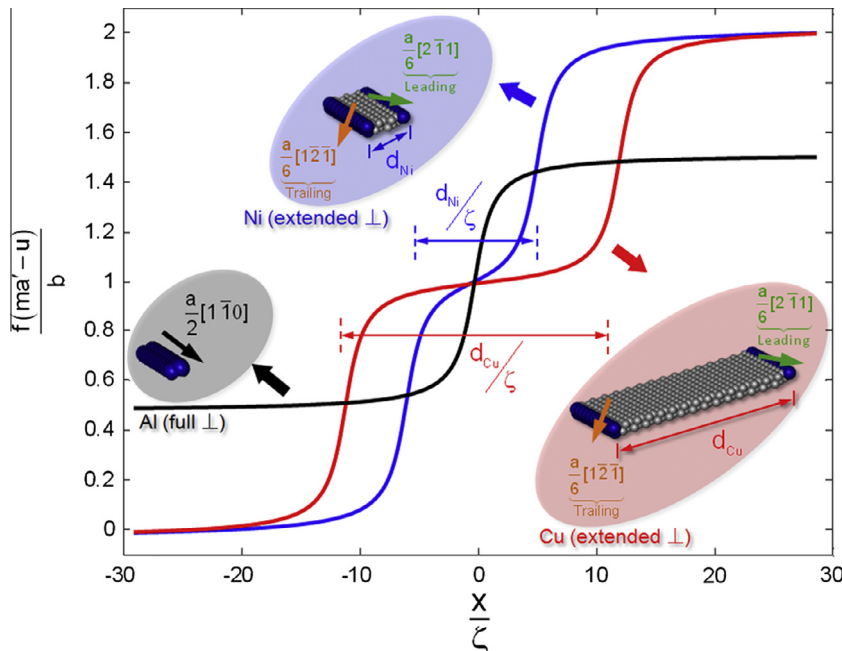


**Fig. 8a.** Disregistry for full (for Al) and extended (for Ni and Cu) dislocations (computed with Eqs. (6) and (7) respectively). The greater partial separation distance in Cu ( $d_{Cu}$ ), compared to Ni ( $d_{Ni}$ ) and Al (no separation) has been highlighted. The disregistry distribution acts as input to Peierls–Nabarro model for calculation of frictional resistance stress,  $\tau_p$  (Peierls stress).

3.4. Calculation of Peierls stress,  $\tau_p$

The Peierls–Nabarro model provides the theoretical framework for predicting crystal impedance to slip motion, which is a strong function of material, dislocation type and bond directionality. The model assumes that the introduction of a dislocation in an otherwise perfect crystal generates two types of energy contribution – elastic (long-ranged) and misfit (short-ranged) [22–24]. The elastic energy accounts for the stretching of bonds surrounding the dislocation core. On the other hand, the misfit energy (denoted by  $E_{misfit}$  or  $E_\gamma^s$ ) is the total energy expenditure for dislocation glide on a particular slip plane along a slip direction. The Peierls stress,  $\tau_p$  i.e. lattice frictional resistance is proportional to the maximum slope of the  $E_\gamma^s$  versus dislocation position,  $u$ , curve (Eq. (4)).

$$\tau_p = \max \left\{ \frac{1}{b} \frac{dE_\gamma^s}{du} \right\} \quad (4)$$

where  $b$  is the Burgers vector.  $E_\gamma^s$  can be obtained by the discrete summation of the area underneath a  $\gamma$  surface as in Eq. (5) (for a full dislocation in Al and extended dislocations in Ni and Cu) as previously obtained from atomistic simulations.

$$E_\gamma^s = \sum_{x=-\infty}^{x=+\infty} \gamma(f(x))a' \quad (5)$$

where  $a'$  is the lattice periodicity i.e. shortest distance between two equivalent atomic rows in Burgers vector direction ( $a' = a/\sqrt{2}$  and

$a' = 2a/\sqrt{6}$  for full and dissociated dislocations respectively);  $f(x) = f(ma' - u)$  is a disregistry function ( $m$  being an integer) that represents relative displacement of atoms across the slip plane. The solution of  $f(x)$  for a full dislocation is given by Eq. (6) [22]. For extended dislocations (as in Ni or Cu) with a partial separation distance  $d$ ,  $f(x)$  is expressed as in Eq. (7) [24].

$$f_{full}(ma' - u) = \frac{b_{full}}{2} + \frac{b_{full}}{\pi} \tan^{-1} \left( \frac{ma' - u}{\zeta} \right) \quad (6)$$

$$f_{extended}(ma' - u) = b_{partial} + \frac{b_{partial}}{\pi} \left[ \tan^{-1} \left( \frac{ma' - u}{\zeta} \right) + \tan^{-1} \left( \frac{ma' - u - d}{\zeta} \right) \right] \quad (7)$$

where  $\zeta$  is the dislocation core half-width which is a function of interplanar distance of the slip planes ( $\zeta_{screw} = a/2\sqrt{3}$  and  $\zeta_{edge} = a/2\sqrt{3}(1 - \nu)$ ,  $\nu$  being the Poisson's ratio) [22];  $b_{full}$  and  $b_{partial}$  are the Burgers vectors for full and Shockley partial dislocations respectively. The Fig. 8a shows a composite plot of disregistry functions for Al (full dislocation), Ni and Cu (extended dislocations). The widths of extended cores for the case of dissociated dislocations in Ni and Cu are highlighted in the plots. The fact that a dissociated dislocation in Cu is characterized by longer stacking fault width compared to that of Ni is also modeled by the respective disregistry functions for Cu and Ni.

The GSFE for a full dislocation with  $b = a/\sqrt{2}$  could be modeled by a single Cosine function, and hence Eq. (5) could be rewritten as follows (Eq. (8)) [25].

$$E_\gamma^s = \sum_{m=-\infty}^{m=+\infty} \frac{\gamma_{us}}{2} \left[ 1 - \cos \frac{2\pi f_{full}}{b} \right] a' \quad (8)$$

For a dissociated dislocation, the GSFE curves could be fitted by multiple Cosine functions, following the approach devised by Wang et al. [26]. Hence, Eq. (5) for extended dislocations with two Shockley partial could be expanded in the form of Eq. (9).

$$E_\gamma^s = \sum_{m=-\infty}^{m=0} \frac{\gamma_{us}}{2} \left[ 1 - \cos \frac{2\pi f_{extended}}{b} \right] a' + \sum_{m=-\infty}^{m=0} \frac{\gamma_{us} - \gamma_{isf}}{2} \left[ 1 - \cos \frac{2\pi f_{extended}}{b} \right] a' + \sum_{m=1}^{m=+\infty} \frac{\gamma_{us} - \gamma_{isf}}{2} \left[ 1 - \cos \frac{2\pi f_{extended}}{b} \right] a' + \sum_{m=1}^{m=+\infty} \frac{\gamma_{us}}{2} \left[ 1 - \cos \frac{2\pi f_{extended}}{b} \right] a' \quad (9)$$

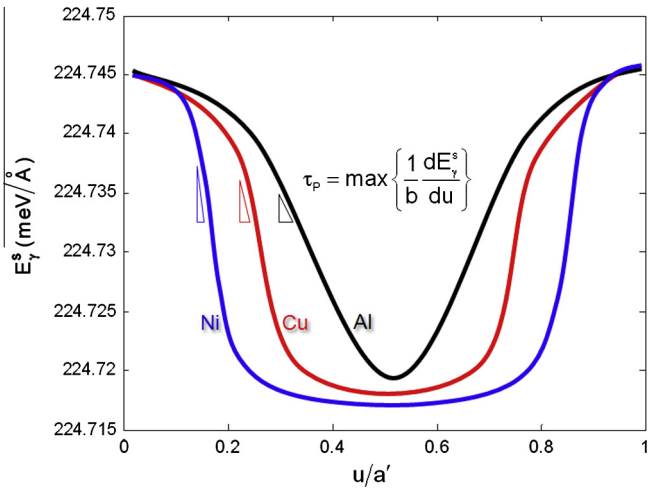


Fig. 8b. Misfit energy,  $E_\gamma^s$ , calculated for Al using Eq. (8) and Ni and Cu from Eq. (9). The maximum slopes of these curves normalized by respective Burgers vectors,  $b$  provide the Peierls stress,  $\tau_p$ .  $E_\gamma^s$  is periodic in nature with a lattice periodicity of  $a'$  ( $b_{full}$  and  $2b_{partial}$  for full and partial dislocations respectively in fcc lattice).

Table 3

Ideal shear strength  $\tau_{max}$ , Peierls stress  $\tau_p$ , and experimental critical resolved shear stress  $\tau_{CRSS}$  for Ni, Cu and Al single crystals.

Dislocation glide condition	Type	Ideal shear strength, $\tau_{max} = \max \left\{ \frac{d\tau}{dx} \right\}$ (GPa)			Peierls stress, $\tau_p = \max \left\{ \frac{1}{b} \frac{dE_\gamma^s}{du} \right\}$ (MPa)			Experimental critical resolved shear stress, $\tau_{CRSS}$ (MPa)		
		Ni	Cu	Al	Ni	Cu	Al	Ni	Cu	Al
Unobstructed (Standard GSFE)	Edge	6	3.58	3.13	9.1	1.19	0.88	9–13.5 [30,31,37,39,43]	2.1–3.2 [27,28,34,40,42,44]	0.78–1.3 [29,32,33,35,36,38,41]
	Screw				10	3	1.2			
Forward transmission (CTB-influenced GSFE)	Edge	12.6	8.3	7.6	9.7	1.56	1.11			
	Screw				10.9	3.18	1.23			
Reverse transmission (CTB- & $b_r$ -influenced GSFE)	Edge	15.9	11.2	9.2	10.35	2.7	2.41			
	Screw	21.3	16.2	11.6	11.88	3.88	2.73			

In Fig. 8b, the misfit energy  $E_{\gamma}^{\text{e}}$  for free dislocation glide for Ni, Cu and Al are plotted together. In the present study, the Peierls stresses for both unobstructed and obstructed (twin boundary-induced) glide have been computed utilizing the above-mentioned approach. In order to extract the twin boundary-restricted Peierls stresses (for forward and reverse flow), total misfit energies are calculated from the modified levels of GSFE (i.e. with increased  $\gamma_{us}$ ) using Eqs. (8) and (9). Eq. (4) then provides the extrinsic levels of frictional stresses,  $\tau_p$ . Table 3 lists the computed Peierls stresses along with the ideal shear strengths,  $\tau_{\text{max}}$  (which is the maximum slope of a GSFE curve) and experimental critical resolved shear stresses,  $\tau_{\text{CRSS}}$  for Ni, Cu and Al. It follows that the thus-computed Peierls stresses for free glide possess a good agreement with the experimentally measured critical resolved shear stress in all three materials (Cu, Ni and Al) [27–44]. The current method of using modified/unmodified GSFEs in Peierls–Nabarro formulations provides forward and reverse glide resistance as imposed by the matrix–twin interface. These lattice frictional stresses constitute important ingredients in implementing dislocation glide based fatigue crack growth in Part II of this study.

## 4. Discussion

### 4.1. Slip characteristics

In the present simulations, Al dislocations emerge as full while Cu and Ni dislocations are of extended type (i.e. leading and trailing Shockley partials connected by a stacking fault ribbon). The splitting distance for a Cu extended dislocation is larger than that of Ni as shown in Fig. 2b. Classically, the stacking fault width for an extended dislocation is inversely proportional to intrinsic stacking fault energy,  $\gamma_{\text{isf}}$  [22] based on the elastic force balance between two partials. However, recent literature [45] indicates that the  $\gamma_{\text{isf}}$  by itself is an insufficient parameter to dictate whether the prevalent slip type would be full or dissociated. It has been proposed that the dissociation criterion for Al, Cu and Ni could be understood by their respective generalized stacking fault energies (GSFE) [45,46]. In order to rationalize the dissociation characteristics in Ni, Cu and Al, we represent the respective  $\gamma$  surfaces by the ratio between the intrinsic stacking fault energy and unstable fault energy,  $\gamma_{us}$ . The computed  $\gamma_{\text{isf}}$  and  $\gamma_{us}$  values for Ni, Cu and Al are provided in Table 2. The  $\gamma_{us}$  and  $\gamma_{\text{isf}}$  values for these materials are found to be in good agreement with density functional theory [47–50] and experimental results [51,52] respectively.

Rice [53] first proposed that the peak energy in a GSFE plot (i.e. unstable stacking fault energy,  $\gamma_{us}$ ) is the barrier for slip nucleation. Considering the case of an extended dislocation, the leading Shockley partial has to overcome  $\gamma_{us}$  as in Fig. 5b. The glide of this leading partial creates a plane of stacking fault in the wake with a fault energy of  $\gamma_{\text{isf}}$ . The width of this stacking fault plane depends on energy balance between the mutual elastic repulsion and the total fault energy. Essentially, the relevant energy barrier for the trailing partial to overcome is now ( $\gamma_{us} - \gamma_{\text{isf}}$ ). In other words, large difference between  $\gamma_{\text{isf}}$  and  $\gamma_{us}$  facilitates widening of partial splitting. Therefore, a lower  $\gamma_{\text{isf}}/\gamma_{us}$  ratio in any material would indicate a greater propensity towards dissociation into partials with increased separation between partials. The  $\gamma_{\text{isf}}/\gamma_{us}$  ratios for Al, Ni and Cu are calculated to be 0.75, 0.50 and 0.23 respectively which are in good agreement with literature value [45]. Consequently, Cu dislocations are found to have wider separation compared to Ni while Al dislocations remain as full. Earlier experimental literature [54,55] have confirmed the observation of type  $\frac{a}{2}\langle 110 \rangle$  full dislocations in cyclically deformed Al. The simulation-related findings are summarized in Table 2.

### 4.2. Cyclic saturation

Early experimental observations [56] have established that fcc single crystals achieve a saturated stress–strain response upon several hundred cycles of load reversal. Microscopically, such cyclic saturation corresponds to a dynamic equilibrium of localized dislocation activities. The sub-structure dislocation arrangement under cyclic equilibrium is experimentally found to be a function of resolved plastic shear strain amplitude (which is typically less than 1% for these experiments) and pre-deformation dislocation density. Depending on these factors, the evolution of stress–strain response may undergo hundreds of cycles, before attaining a steady state microstructure. However, in the present molecular dynamics simulations, a strain range as high as 13% has been applied on pristine nano-twinned single crystals with no prior presence of dislocations (in Cu, Ni and Al) in order to expedite the saturation state due to limited computational capability. As such, it has been observed that the simulation stress–strain response attains a steady-state behavior, upon mere four cycles of load reversal as shown in Figs. 3a and 3b.

At the micro-scale, the nature of cyclic slip–twin boundary reaction reaches a recurrent pattern. The saturated dislocation arrangements for edge and screw cases differ in terms of gradual evolution of residual dislocation on the boundary. For the edge case, no net residual dislocation density change on the twin boundary occurs over a cycle as the sessile residual dislocation is eliminated during the reverse flow. On the other hand, for the screw case, residual twinning partial dislocations glide farther away from the reaction site, causing twin migration (i.e. growth or shrinkage of the twin by one atomic layer) on each cycle. Twin migration process itself does not alter the local atomic arrangement i.e. the coherency of the twin boundary. Therefore, on subsequent cycles, an incident dislocation encounters an unvaried matrix–twin interface, and undergoes identical interaction mechanism. Hence, it could be reasonably deduced that, given hundreds of cycles, the observed saturation effect as a consequence of cyclic slip–twin interaction would not be significantly different from the present observation.

### 4.3. Cyclic slip–twin boundary interaction

Li et al. [57] have established the conditions regarding the outcomes of slip–boundary reactions as – (i) maximization of local resolved shear stress, (ii) minimization of angle between incoming and outgoing slip plane and (iii) minimization of residual Burgers vector,  $b_r$  – known as the so-called LRB criterion. Based on the LRB criterion, the intersection of an incident dislocation and a boundary can occur via two fundamentally distinct mechanisms [8,58,59] – (a) incorporation of incident dislocation on the interface (i.e. complete blockage of oncoming slip) and (b) direct transmission with or without any residual dislocation [9,58]. In the present simulations, a screw and an edge dislocation transfers inside the twin leaving a sessile Frank partial and a pair of gliding twinning partials respectively as net residual dislocation. Such outcomes could be rationalized by examining the local stress state given by Schmid factors. Under pure shear loading ( $\tau_{13}$  or  $\tau_{23}$ ), the Schmid factor is defined as the ratio between the resolved shear stress,  $\tau_{\text{RSS}}$  and the Tresca definition of applied stress,  $\tau_{\text{Tresca}} (= 2\tau_{13}$  or  $2\tau_{23})$ . This description of Schmid factor is consistent with the traditional definition in literature (for example, for uniaxial tension,  $\tau_{\text{Tresca}} = \sigma_{11}$ ). Under  $\tau_{13}$  shear (which corresponds to the screw dislocation case), the maximum Schmid factor of 0.5 exists on the twin boundary plane for the single crystal configuration shown in Fig. 2a. Hence, for the screw case, such high magnitude of acting resolved shear stress on the twin boundary is conducive to the nucleation of glissile twinning partials. By contrast, no resolved shear stress exists on the twin boundary slip systems under  $\tau_{23}$  loading i.e. zero Schmid factor (the edge dislocation case). Therefore, the interaction between the oncoming edge dislocation

and the boundary culminates in the generation of sessile Frank type residual dislocation since the local stress does not provide any acting component for shearing on the twin boundary. Table 1 summarizes the slip–twin boundary interactions for the edge and screw cases.

Experimental literature note that it is possible to have different slip–twin interactions, depending on a favorable combination of dislocation geometry and Schmid factors [9,10,57,60] as dictated by the LRB criterion. For instance, in transmission electron micrographs, screw dislocations are observed to have transferred into the twin via simple cross-slipping without generating any residual dislocation. It is also possible to have mixed dislocations impinging on the twin, leading to different reaction products than the current observation. Nevertheless, the present cases analyzed span two extremities of local stress condition as well as dislocation type (i.e. pure edge and screw). The fundamental differences in the cyclic interfacial plasticity are manifested in the form of irreversibilities of dislocation glide trajectories. Therefore, it can be reasonably deduced that fundamental differences due to any other outcomes of twin boundary–dislocation (e.g. of mixed type) interceptions would essentially lie in different degrees of cyclic slip irreversibilities.

#### 4.4. Cyclic slip irreversibilities

The fatigue damage occurs due to incremental irreversible dislocation activities. Mughrabi [61] utilized the concept of cyclic slip irreversibility in an empirical relationship to model total fatigue life based on available experimental data. Pippan [62–64] highlighted the importance of the irreversibility of crack-emitted slip in predicting the threshold of crack propagation. These studies demonstrate that the quantification of cyclic slip irreversibilities can lead to the prediction of macroscopic fatigue damage behavior. Nevertheless, the assessment of the degree of irreversibility has been a challenging task, and associated literature is limited. Existing literature have reported both theoretical and experimental endeavors regarding quantifying the irreversibility factor,  $p$ , with a view to understanding cyclic strain accumulation at the micro-scale [21,61,65,66].

Essmann [21] proposed a model of a persistent slip band (PSB) on the basis of incremental cyclic slip irreversibilities. This model considered the existence of equilibrium between dislocation multiplication and annihilation, resulting in gradual irreversibility. The saturated value of irreversibility factor,  $p$ , was predicted to range from 0.2 to 0.5 depending on the considered dislocation character (edge and screw respectively) in Cu single crystals [21,67]. More recently, Weidner et al. [66] have experimentally measured the irreversibility factor to be 0.8 for a PSB in polycrystalline nickel. These works considered the slip irreversibilities essentially in the context of the evolution of a PSB i.e. a physical process leading to crack initiation. On the other hand, mechanistically, the stable crack propagation is also governed by the degree of cyclic irreversibilities of crack-emitted dislocations [63,68]. The current theoretical assessment of  $p$  is performed for the crack-emitted slip irreversibilities influenced by a twin presented in Figs. 4a and 4b.

We show that the irreversibility factor associated with crack-tip slip phenomena is correlated with the nano-dimensions of a twin (i.e. lamellar thickness,  $t$  and twin to source distance,  $d$ ). An annealing twin in three different materials (Ni, Cu and Al) has been observed to modify the irreversibility factor to different extents i.e.  $p_{\text{Ni}} < p_{\text{Cu}} < p_{\text{Al}}$  regardless of dislocation character (edge or screw). This trend could be understood in light of the relative lattice frictional stress i.e. Peierls stress,  $\tau_p$ , in Ni, Cu and Al. From Table 3, the theoretical Peierls stress as well as experimental critical resolved shear stress follow the order of  $\tau_p^{\text{Ni}} > \tau_p^{\text{Cu}} > \tau_p^{\text{Al}}$ . We note that the degree of irreversibility in the present case is demonstrably dictated by the dislocation glide impedance. Easy glide condition is found to favor higher irreversibilities whereas increased

glide resistance leads to reduced levels of  $p$ . Mechanistically, the different levels of frictional stresses have been observed to influence the location of dislocation annihilation, thereby modifying the irreversible glide trajectories.

The insets of Figs. 4a and 4b pictorially illustrate the distance between the annihilation spot (designated  $f$ ) and the crack-tip location (designated  $a$ ) with varying twin lamellar thickness,  $t$  or source to twin distance,  $d$ . The annihilation spot shifts away from the source, with increasing  $d$  or  $t$ . In the simulations, a twin with increased  $t$  or  $d$  necessitates a larger external load in order for the source-emitted dislocations to reach the nearest twin boundary. This results in a gradually larger number of slip nucleation from the source. The saturated  $p$  levels correspond to the involvement of multiple dislocations, when annihilation occurs at a fixed location independent of twin nano-dimensions. On the other hand, for smaller  $t$  and/or  $d$ , trajectories for returning dislocations are more reversible. They annihilate in close proximity to the source owing to limited volume available for dislocations of opposite sign to glide farther. Experimentally, reversible flow of pure edge dislocation, upon interacting with grain boundaries, has been reported by Mompou et al. [69] in Al.

It is important to note that the irreversibility factor levels computed in the present work are rather high compared to literature experimental values [21,64–66]. This could be understood in view of the facts that literature data are considered for PSBs at low plastic strain amplitude. It has been found that slip irreversibility factor,  $p$  is strongly dependent on local plastic shear strain amplitude [65]. As clarified earlier, the current computational limitations preclude conducting hundreds of deformation cycle simulations under plastic strain amplitudes comparable to experiments. Nonetheless, the aforementioned trends bear important implications regarding the influences of these twin related nano-dimensions on crack advance mechanism.

#### 4.5. Unstable stacking fault energy ( $\gamma_{us}$ )

The quantification of  $\gamma_{us}$  variations near a coherent twin boundary (CTB) and/or residual dislocation,  $\vec{b}_r$  has provided an energy-based measure of relative glide resistances for forward and reverse flow as affected by these obstacles (Figs. 6a, 6b and 6c). Apart from the inherent lattice friction (represented by the bulk  $\gamma_{us}$  values at the points A, A' and C), a dislocation slip needs to overcome additional stresses associated with the CTB (at B) and  $\vec{b}_r$  (at D and E). The stress concentrations (around a CTB or a  $\vec{b}_r$  for edge case as shown in Figs. 7a and 7b respectively) induce an elevation in the  $\gamma_{us}$  levels from its bulk values. It has been observed that the increase in  $\gamma_{us}$  at the matrix–twin interface is proportional to the magnitude of  $\vec{b}_r$ . The incident screw dislocation ( $|\vec{b}_r|_{\text{screw}} = \frac{a}{\sqrt{2}}$ ) has to overcome a greater energy barrier compared to the edge dislocation ( $|\vec{b}_r|_{\text{edge}} = \frac{a}{\sqrt{3}}$ ). As demonstrated, in any case, reverse glide past the interface encounters enhanced energy barriers compared to the forward flow. The discrepancy in the relative resistances to forward and reverse slip triggers a chain of events, ultimately leading to the annihilation process. It follows that a greater resolved shear stress would be required for the returning dislocations to re-enter the matrix to overcome the comparatively high energy barrier. This, in turn, necessitates an increase in the farfield applied loading to transfer slip back into the matrix during reverse loading. The source-bound dislocations, experiencing enhanced impedance to glide, are temporarily halted at the CTB, while newly-nucleated negative dislocations can continue to glide gradually farther from the source. As a result, the dislocation annihilation spot moves farther away from the source, resulting in an increased total irreversible shear strain components. The energy pathway plots act to provide a physical rationale for the events leading to irreversibility of cyclic glide paths. Moreover, the modified  $\gamma$  surfaces, corresponding to the enhanced  $\gamma_{us}$  at B, D and E, act as input to the calculation of increased Peierls stress  $\tau_p$  for dislocation glide past a CTB.

#### 4.6. Lattice frictional stress

Metallic lattice provides periodic resistance to dislocation glissile motion. Such resistance forces originate from a periodic energy profile along a specific crystallographic direction on a certain slip plane, most accurately described by  $\gamma$  surfaces or generalized stacking fault energy (GSFE) plots. The maximum slope of a GSFE curve ( $\frac{d\gamma}{dx}$ ) corresponds to the ideal shear strength (as denoted by  $\tau_{\max}$ ) of the material i.e. the stress necessary to shear a crystal by simultaneously breaking all the bonds across the shear plane. The level of  $\tau_{\max}$  is on the order of several gigapascals. It follows from Table 3 that Ideal shear strength,  $\tau_{\max}$  increases to a considerable degree for twinned single crystals. Such variation is related to corresponding local variation of GSFE (in the form of increased  $\gamma_{us}$ ) at twin boundaries. The substantial increase in  $\tau_{\max}$  may be attributed to non-linear contribution of concentrated stresses associated with an interface and/or the residual dislocation. It poses as a topic of further research to refine the understanding of correlation between  $\gamma_{us}$  and the degree of stress concentrations. However, for ductile material, nucleation of slip reduces material strength against shearing by several orders of magnitude. Peierls–Nabarro model provides a theoretical framework to predict lattice resistance stress to slip (i.e. Peierls stress,  $\tau_p$ ). Peierls stress depends not only upon the nature of  $\gamma$  surface but also dislocation core geometry (i.e. extended versus narrow core) and nature of lattice registry around the core [70].

The nature of the crystal periodicity strongly dictates the degree of resistance to dislocation glissile motion. The predictive capability of the Peierls–Nabarro model, therefore, relies on the precise description of these  $\gamma$  surfaces [70]. In the present work, we have employed a Peierls–Nabarro based methodology where extrinsic levels of GSFE plots, as modified by local stress contribution, have been utilized to compute the total misfit energy. The calculation of total misfit energy from the unmodified and/or modified GSFE plots facilitates the extraction of Peierls stresses (which is the maximum slope of misfit energy versus dislocation position curve as in Fig. 8b). This approach, thereby, facilitates the quantification of increased levels of dislocation glide resistance as imposed by the CTB- and  $b_r$ -associated local stress concentrations. We validate thus-computed frictional stress levels by observing that the current approach provides reasonable agreement of Peierls stresses for unobstructed glide with experimentally determined critical resolved shear stresses,  $\tau_{CRSS}$  for pure Ni, Cu and Al (in Table 3).

The frictional stress data in Table 3 will be utilized in a continuum fatigue crack growth simulation. In particular, the computed differential in the Peierls stresses at a twin boundary in Ni, Cu and Al will be used to trigger irreversibilities of crack-emitted slip under mode I, II and III loadings. The model is described in Part II of the study.

## 5. Conclusions

The primary objective of the present work was to study the mechanistic origin of irreversible slip phenomena underlying fatigue damage propagation. We studied the governing variables at appropriate lengthscales: (i) atomistics – role of annealing twin on slip irreversibilities (ii) mesoscale – lattice frictional stresses as influenced by a twin boundary. The synopsis of major contributions is presented below.

- (1) The present investigation provides detailed analyses of cyclic dislocation–twin boundary interactions considering pure edge and screw dislocations in Ni, Cu and Al. These reactions retain the conservation of Burgers vectors, and generate residual dislocations on the twin boundary. During cyclic flow, dislocations undergo annihilation, thereby creating irreversible glide trajectories. The computed cyclic irrevers-

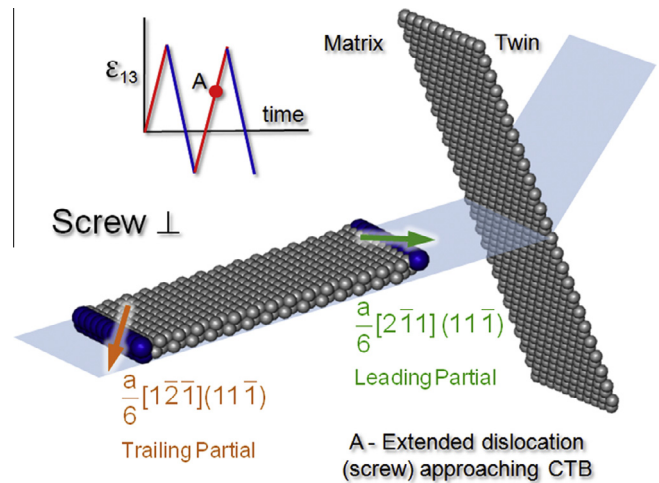


Fig. A1. In Cu, an extended screw dislocation (dissociated into leading partial,  $\frac{a}{6}[2\bar{1}\bar{1}]$  and trailing partial  $\frac{a}{6}[1\bar{2}\bar{1}]$ ) is approaching the matrix–twin interface at an instant of the forward deformation cyclic (marked as A) under  $\varepsilon_{13}$  type straining.

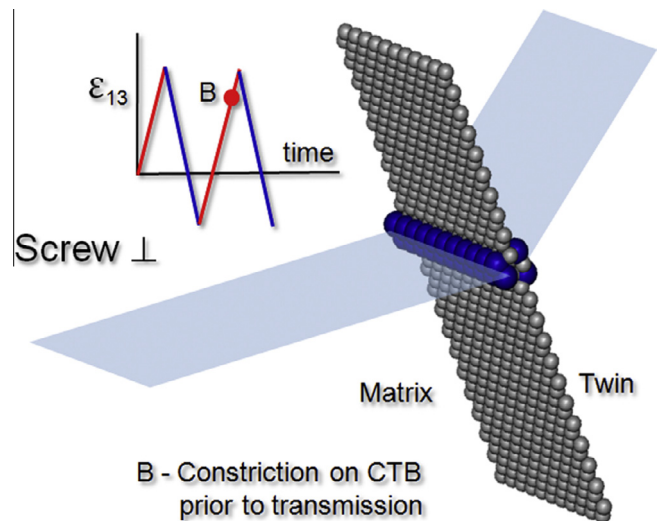


Fig. A2. Upon reaching the coherent twin boundary (CTB) (at point B), the extended dislocation (in Cu) undergoes constriction [71] before transferring inside the twin.

bilities in these materials are found to follow a trend of  $p_{Ni} < p_{Cu} < p_{Al}$ . Mechanistic origin of the irreversibilities is correlated with the trends in dislocation glide impedances manifested in the form of modified generalized stacking fault energies in the respective materials.

- (2) Unstable stacking fault energy,  $\gamma_{us}$ , is found to increase around a twin boundary and residual dislocation due to associated stress concentrations. In particular, the residual dislocation contributes to the irreversibility by increasing the reverse flow resistance. The differential of flow resistances for forward and reverse flow triggers slips irreversibilities. The computed energetics provides a physical rationale for the origin of irreversibility. These energy considerations have subsequently been translated into frictional resistance stresses.
- (3) Peierls–Nabarro based formulations are used to compute lattice frictional stresses for free glide as well twin-restricted glide for forward and reverse plasticity. A database for twin-induced Peierls stresses in Ni, Cu and Al has been established for use in fatigue threshold prediction to be implemented in Part II of the study.

**Acknowledgements**

The support of Honeywell Aerospace Corporation is gratefully acknowledged. We also acknowledge the use of the parallel computing resource, the Taub cluster, at the University of Illinois.

**Appendix A. Screw dislocation interacting with twin boundary**

The crystal in Fig. 2a, upon  $\epsilon_{13}$  shear deformation, generates extended screw dislocations from the source in Cu and Ni. By con-

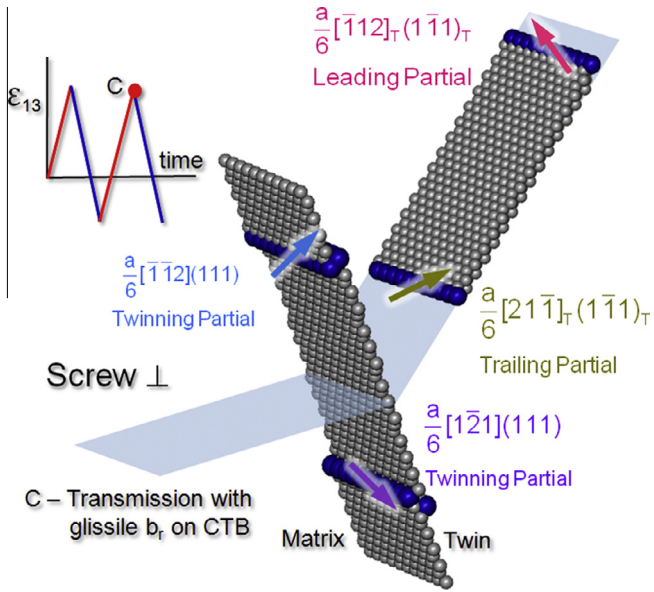


**Fig. A3.** At the end of the  $\epsilon_{13}$  forward straining (at point C), the interaction between the CTB and incident dislocation resulted in transmission of one extended dislocation (leading  $\frac{a}{6}[112]_T$  and trailing  $\frac{a}{6}[211]_T$ ) inside the twin and a pair of twinning partials ( $\frac{a}{6}[112]$  and  $\frac{a}{6}[121]$ ) on the CTB. The twinning partials glide away from each other, resulting in the migration of twin thickness by one atomic layer on twinning plane (111).

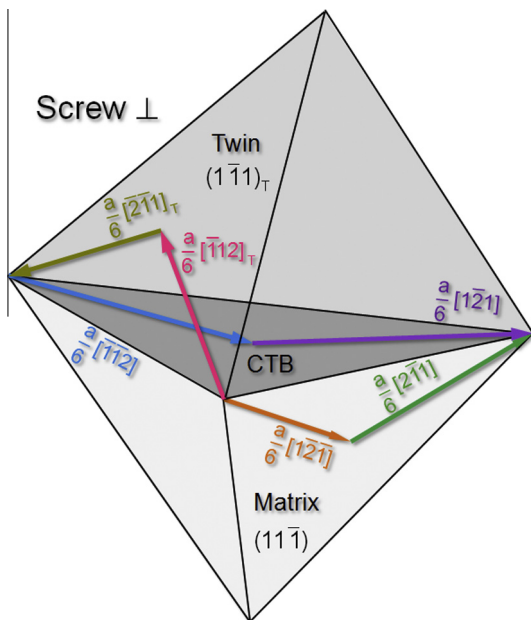


**Fig. A4.** A double Thompson tetrahedron representation of the matrix and twin activated slip systems describing the forward reaction for the case of an incident dislocation of screw type.

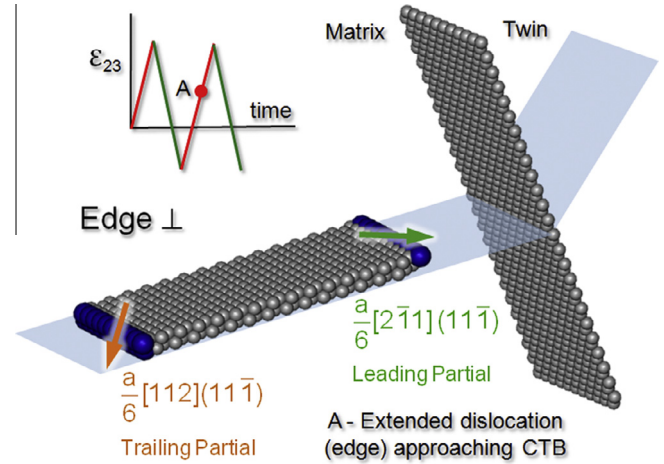


**Fig. B1.** At the loading point A, an extended edge dislocation (dissociated into leading partial,  $\frac{a}{6}[211]$  and trailing partial  $\frac{a}{6}[112]$ ) is approaching the nearest twin boundary during the forward deformation cyclic under  $\epsilon_{23}$  type loading.

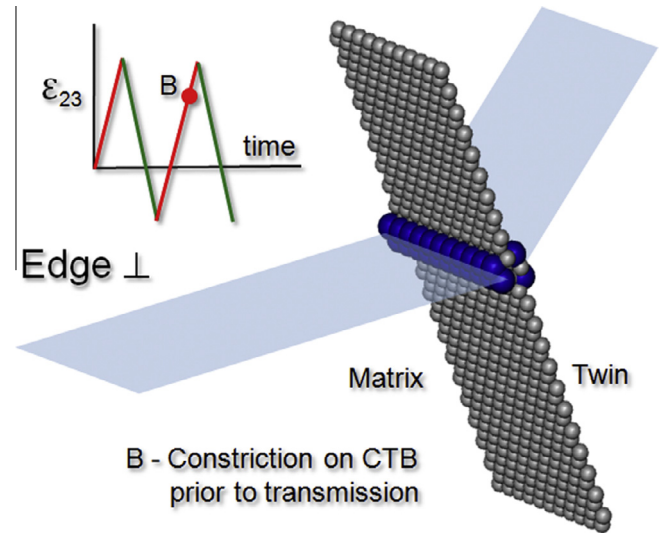


**Fig. B2.** The incident extended edge dislocation (in Cu) constricts to a total dislocation  $[\bar{7}1]$  prior to the transmission inside the twin.

trast, no dissociation is observed in Al, emergent dislocation being of type  $\frac{a}{2}[1\bar{1}0]$ . Fig. A1 depicts an incident leading Shockley partial,  $\frac{a}{6}[211]$  (followed by a trailing partial,  $\frac{a}{6}[121]$ ) in Cu, approaching the twin boundary (at point A). The dissociation reaction both for Cu and Ni (edge and screw) is identical and given by Eq. (A1).

$$\frac{a}{2} [\bar{1}\bar{1}0]_{\text{Full(screw)}} \rightarrow \frac{a}{6} [2\bar{1}1]_{\text{Leading}} + \frac{a}{6} [1\bar{2}\bar{1}]_{\text{Trailing}} + \text{Stacking Fault} \quad (\text{A1})$$

Fig. A2 shows that, the partials both in Cu and Ni constrict to form a full dislocation at B (via Friedel–Esaig type constriction mechanism [71]), and align onto the boundary. In Fig. A3, at the end of the forward straining (at C), an extended dislocation transmits inside the twin, leaving a pair of glissile twinning partials (incorporation reaction) as a net residual dislocation,  $b_r$ . These incorporated twinning partials cause twin migration by one atomic layer, resulting in either growth or shrinkage of the twin. Eq. (A2) summarizes this reaction for Cu and Ni. On the other hand, the forward reaction in Al differs, in that the incident and transferred dislocations are perfect dislocations of  $\frac{a}{2}[1\bar{1}0]$  type with the same net

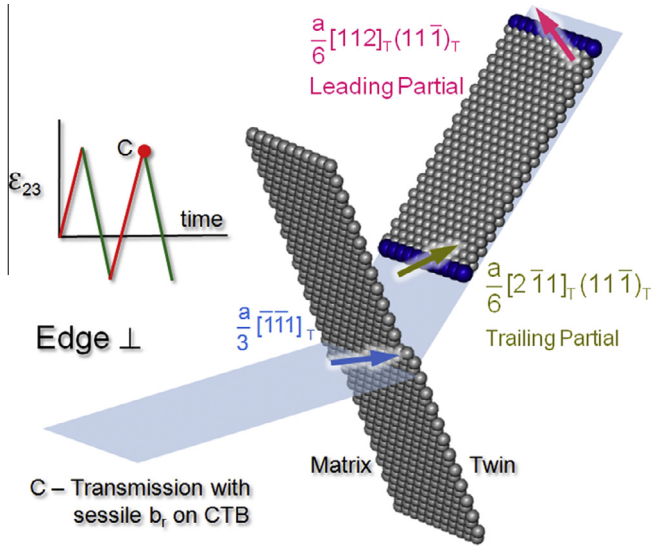


**Fig. B3.** At point C reaching the end of the  $\epsilon_{23}$  forward straining, incident edge dislocation–boundary interaction led to the transmission of one extended dislocation (leading  $\frac{a}{6}[112]_T$  and trailing  $\frac{a}{6}[2\bar{1}1]_T$ ) inside the twin and a sessile Frank partial of type  $\frac{a}{3}[\bar{1}11]_T$  is left on the interface.

$b_r$  (Eq. (A3)). In Eqs. (A2) and (A3), the total Burgers vector is conserved if all the vectors are represented in the same frame (either matrix or twin). The forward reaction is presented with a double Thompson's tetrahedron for the partial case in Fig. A4.

$$\underbrace{\frac{a}{6}[2\bar{1}1]}_{\text{Leading}} + \underbrace{\frac{a}{6}[12\bar{1}]}_{\text{Trailing}} \rightarrow \underbrace{\frac{a}{6}[\bar{1}12]}_{\text{Twinning}} + \underbrace{\frac{a}{6}[12\bar{1}]}_{\text{Twinning}} + \underbrace{\frac{a}{6}[2\bar{1}1]_T}_{\text{Trailing}} + \underbrace{\frac{a}{6}[\bar{1}12]_T}_{\text{Leading}} \quad (\text{A2})$$

Incident (Matrix)      Incorporated ( $b_r$ )      Transmitted (Twin)

$$\underbrace{\frac{a}{2}[\bar{1}10]}_{\text{Full}} \rightarrow \underbrace{\frac{a}{6}[\bar{1}12]}_{\text{Twinning}} + \underbrace{\frac{a}{6}[12\bar{1}]}_{\text{Twinning}} + \underbrace{\frac{a}{2}[\bar{1}01]_T}_{\text{Full}} \quad (\text{A3})$$

Incident (Matrix)      Incorporated ( $b_r$ )      Transmitted (Twin)

Upon reversal of load, the transmitted dislocation from within the twin approaches the interface. The inset of Fig. 3a in the main text illustrates the overall dislocation arrangement at the end of the reverse straining (designated by R). The twinning partials at positions c and e are from the forward reaction, and those at c' and e' from the reverse incidence. The new twinning partials at c' and e' repulse the ones at c and e, thereby forcing them to still glide in forward direction even against the acting reverse shear stress. The arrows show their motion directions. One dislocation re-emerges into the matrix, and continues its glide towards the source. This dislocation encounters a newly nucleated dislocation of opposite sign from the source, and they annihilate each other.

**Appendix B. Edge dislocation interacting with twin boundary**

The interaction of an edge dislocation (full or dissociated) with a twin boundary differs only in the form the type of the net residual dislocation,  $b_r$ . Figs. B1–B3 illustrate the forward sequence for

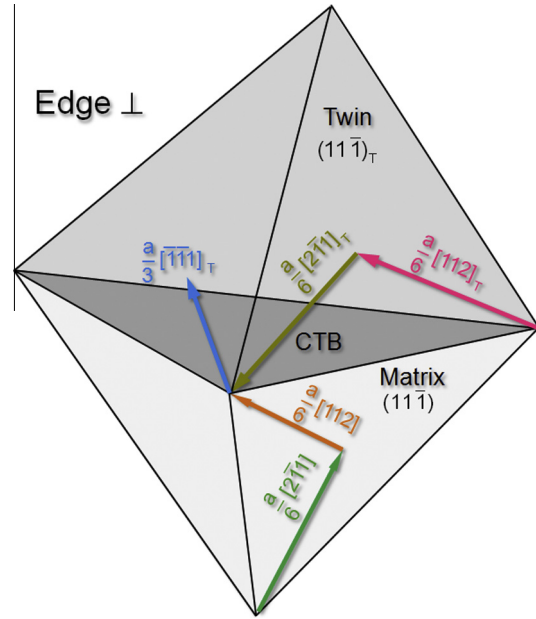


**Fig. B4.** The double Thompson tetrahedron representation of the activated slip systems (matrix and twin) depicting the forward reaction for the case of an edge dislocation impingement on the coherent twin boundary (CTB).

the case of an extended dislocation ( $\frac{a}{6}[112]$  leading and  $\frac{a}{6}[2\bar{1}1]$  trailing Shockley partials) in Cu. The  $b_r$  is a Frank partial type sessile dislocation on the twin boundary, unlike the glissile twinning partials for the screw case. Eqs. (B1) and (B2) summarize the reactions for dissociated and full dislocations respectively. A Double Thompson's tetrahedron representation is provided in Fig. B4.

$$\underbrace{\frac{a}{6}[2\bar{1}1]}_{\text{Leading}} + \underbrace{\frac{a}{6}[112]}_{\text{Trailing}} \rightarrow \underbrace{\frac{a}{3}[\bar{1}11]_T}_{\text{Sessile } b_r} + \underbrace{\frac{a}{6}[112]_T}_{\text{Trailing}} + \underbrace{\frac{a}{6}[2\bar{1}1]_T}_{\text{Leading}} \quad (\text{B1})$$

Incident (Matrix)      Transmitted (Twin)

$$\underbrace{\frac{a}{2}[101]}_{\text{Full}} \rightarrow \underbrace{\frac{a}{3}[\bar{1}11]_T}_{\text{Sessile } b_r} + \underbrace{\frac{a}{2}[101]_T}_{\text{Full}} \quad (\text{B2})$$

Incident (Matrix)      Transmitted (Twin)

During the reverse deformation, the returning dislocation interacts with the  $b_r$ , resulting in the re-emergence of a source-bound matrix dislocation. Similar to the screw case, this dislocation is annihilated by another dislocation of opposite sign from the source. It is noted that the reaction itself at the twin boundary for the edge case is completely reversible. However, the total glide path over a cycle becomes irreversible solely due to annihilation on its return trajectory. The presence of  $b_r$  serves as an enhanced resistance to the returning dislocation, facilitating the nucleation of opposite-signed dislocation. By contrast, for screw case, the total irreversible strain is also contributed by incorporation lengths.

## Appendix C. Supplementary material

Supplementary data associated with this article can be found, in the online version, at <http://dx.doi.org/10.1016/j.ijfatigue.2014.05.014>.

## References

- [1] Suresh S. Fatigue of materials. Cambridge University Press; 1998.
- [2] Afanasyev KA, Sansoz F. Strengthening in gold nanopillars with nanoscale twins. *Nano Lett* 2007;7:2056–62.
- [3] Chen M, Ma E, Hemker KJ, Sheng H, Wang Y, Cheng X. Deformation twinning in nanocrystalline aluminum. *Science* 2003;300:1275–7.
- [4] Kulkarni Y, Asaro RJ. Are some nanotwinned fcc metals optimal for strength, ductility and grain stability? *Acta Mater* 2009;57:4835–44.
- [5] Lu L, Schwaiger R, Shan ZW, Dao M, Lu K, Suresh S. Nano-sized twins induce high rate sensitivity of flow stress in pure copper. *Acta Mater* 2005;53:2169–79.
- [6] Sangid MD, Pataky GJ, Sehitoglu H, Rateick RG, Niendorf T, Maier HJ. Superior fatigue crack growth resistance, irreversibility, and fatigue crack growth-microstructure relationship of nanocrystalline alloys. *Acta Mater* 2011;59:7340–55.
- [7] Singh A, Tang L, Dao M, Lu L, Suresh S. Fracture toughness and fatigue crack growth characteristics of nanotwinned copper. *Acta Mater* 2011;59:2437–46.
- [8] Jin ZH, Gumbsch P, Ma E, Albe K, Lu K, Hahn H, et al. The interaction mechanism of screw dislocations with coherent twin boundaries in different face-centred cubic metals. *Scripta Mater* 2006;54:1163–8.
- [9] Mahajan S, Chin GY. Twin–slip, twin–twin and slip–twin interactions in Co–8 wt.% Fe alloy single crystals. *Acta Metall* 1973;21:173–9.
- [10] Remy L. Twin-slip interaction in fcc crystals. *Acta Metall* 1977;25:711–4.
- [11] Frenkel D, Smit B, Ratner MA. Understanding molecular simulation: from algorithms to applications. *Phys Today* 1997;50:66.
- [12] Plimpton S. Fast parallel algorithms for short-range molecular dynamics. *J Comput Phys* 1995;117:1–19.
- [13] Tadmor EB, Miller RE. Modeling materials: continuum, atomistic and multiscale techniques. Cambridge University Press; 2011.
- [14] Mishin Y, Mehl MJ, Papaconstantopoulos DA, Voter AF, Kress JD. Structural stability and lattice defects in copper: ab initio, tight-binding, and embedded-atom calculations. *Phys Rev B* 2001;63:224106.
- [15] Foiles SM, Hoyt JJ. Computation of grain boundary stiffness and mobility from boundary fluctuations. *Acta Mater* 2006;54:3351–7.
- [16] Mishin Y, Farkas D, Mehl MJ, Papaconstantopoulos DA. Interatomic potentials for monoatomic metals from experimental data and ab initio calculations. *Phys Rev B* 1999;59:3393.
- [17] Zhou M. A new look at the atomic level virial stress: on continuum–molecular system equivalence. *Proc Roy Soc Lond A: Math Phys Eng Sci* 2003;459:2347–92.
- [18] Humphrey W, Dalke A, Schulten K. VMD: visual molecular dynamics. *J Mol Graph* 1996;14:33–8.
- [19] Li J. AtomEye: an efficient atomistic configuration viewer. *Modell Simul Mater Sci Eng* 2003;11:173.
- [20] Chowdhury PB, Sehitoglu H, Rateick RG, Maier HJ. Modeling fatigue crack growth resistance of nanocrystalline alloys. *Acta Mater* 2013.
- [21] Essmann U. Irreversibility of cyclic slip in persistent slip bands of fatigued pure fcc metals. *Philos Mag A* 1982;45:171–90.
- [22] Hirth JP, Lothe J. Theory of dislocations. 2nd ed. New York: McGraw-Hill; 1982.
- [23] Joos B, Duesbery MS. The Peierls stress of dislocations: an analytic formula. *Phys Rev Lett* 1997;78:266–9.
- [24] Schoeck G. The generalized Peierls–Nabarro model. *Philos Mag A* 1994;69:1085–95.
- [25] Tadmor EB, Miller RE. Modeling materials: continuum, atomistic and multiscale techniques. Cambridge University Press; 2011.
- [26] Wang J, Sehitoglu H, Maier HJ. Dislocation slip stress prediction in shape memory alloys. *Int J Plast* 2013.
- [27] Adams MA, Cottrell AH. CXXXI. Effect of temperature on the flow stress of work-hardened copper crystals. *Phil Mag* 1955;46:1187–93.
- [28] Blewitt TH. Deformation of copper single crystals at 300 K and 78 K. *Phys Rev* 1953;91:1115.
- [29] Cottrell AH, Stokes RJ. Effects of temperature on the plastic properties of aluminium crystals. *Proc R Soc Lond A* 1955;233:17–34.
- [30] Gottstein G, Kocks UF. Dynamic recrystallization and dynamic recovery in (111) single crystals of nickel and copper. *Acta Metall* 1983;31:175–88.
- [31] Haasen P. Plastic deformation of nickel single crystals at low temperatures. *Phil Mag* 1958;3:384–418.
- [32] Hosford Jr WF, Fleischer RL, Backofen WA. Tensile deformation of aluminum single crystals at low temperatures. *Acta Metall* 1960;8:187–99.
- [33] Howe S, Liebmann B, Lucke K. High temperature deformation of aluminum single crystals. *Acta Metall* 1961;9:625–31.
- [34] Jackson PJ, Basinski ZS. Latent hardening and the flow stress in copper single crystals. *Can J Phys* 1967;45:707–35.
- [35] Jaoul PB. Etude de la forme des courbes de deformation plastique. *J Mech Phys Solids* 1957;5:95–102.
- [36] Kocks UF, Brown TJ. Latent hardening in aluminum. *Acta Metall* 1966;14:87–98.
- [37] Latanision RM, Staehle RW. Plastic deformation of electrochemically polarized nickel single crystals. *Acta Metall* 1969;17:307–19.
- [38] Maddin R, Cottrell AH. LXXXIII. Quench hardening in aluminium single crystals. *Phil Mag* 1955;46:735–43.
- [39] Mader S, Seeger A, Leitz C. Work hardening and dislocation arrangement of FCC single crystals. I. Plastic deformation and slip line studies of nickel single crystals. *J Appl Phys* 1963;34:3368–75.
- [40] Seeger A, Diehl J, Mader S, Rebstock H. Work-hardening and work-softening of face-centred cubic metal crystals. *Phil Mag* 1957;2:323–50.
- [41] Staubwasser W. On work-hardening of aluminium-single crystals (99.99%) and its interpretation. *Acta Metall* 1959;7:43–50.
- [42] Thornton PR, Mitchell TE, Hirsch PB. The strain-rate dependence of the flow stress of copper single crystals. *Phil Mag* 1962;7:337–58.
- [43] Windle AH, Smith GC. The effect of hydrogen on the plastic deformation of nickel single crystals. *Metal Sci* 1968;2:187–91.
- [44] Young FW. On the yield stress of copper crystals. *J Appl Phys* 1962;33:963–9.
- [45] Van Swygenhoven H, Derlet PM, Froseth AG. Stacking fault energies and slip in nanocrystalline metals. *Nat Mater* 2004;3:399–403.
- [46] Froseth AG, Derlet PM, Van Swygenhoven H. Dislocations emitted from nanocrystalline grain boundaries: nucleation and splitting distance. *Acta Mater* 2004;52:5863–70.
- [47] Lu G, Kiousis N, Bulatov VV, Kaxiras E. Generalized-stacking-fault energy surface and dislocation properties of aluminum. *Phys Rev B* 2000;62:3099.
- [48] Ogata S, Li J, Yip S. Ideal pure shear strength of aluminum and copper. *Science* 2002;298:807–11.
- [49] Shang SL, Wang WY, Wang Y, Du Y, Zhang JX, Patel AD, et al. Temperature-dependent ideal strength and stacking fault energy of fcc Ni: a first-principles study of shear deformation. *J Phys: Condens Matter* 2012;24:155402.
- [50] Siegel DJ. Generalized stacking fault energies, ductilities, and twinnabilities of Ni and selected Ni alloys. *Appl Phys Lett* 2005;87:121901–3.
- [51] Carter CB, Holmes SM. The stacking-fault energy of nickel. *Phil Mag* 1977;35:1161–72.
- [52] Stobbs WM, Sworn CH. The weak beam technique as applied to the determination of the stacking-fault energy of copper. *Phil Mag* 1971;24:1365–81.
- [53] Rice JR. Dislocation nucleation from a crack tip: an analysis based on the Peierls concept. *J Mech Phys Solids* 1992;40:239–71.
- [54] Feltner CE. The mechanism of prismatic dislocation loop formation in cyclically strained aluminium. *Phil Mag* 1966;14:1219–31.
- [55] Mitchell AB, Teer DG. The analysis of dislocation structures in fatigued aluminium single crystals exhibiting striations. *Phil Mag* 1970;22:399–417.
- [56] Mughrabi H. The cyclic hardening and saturation behaviour of copper single crystals. *Mater Sci Eng* 1978;33:207–23.
- [57] Lee TC, Robertson IM, Birnbaum HK. An In Situ transmission electron microscope deformation study of the slip transfer mechanisms in metals. *Metal Trans A* 1990;21:2437–47.
- [58] Zhu T, Li J, Samanta A, Kim HG, Suresh S. Interfacial plasticity governs strain rate sensitivity and ductility in nanostructured metals. *Proc Natl Acad Sci* 2007;104:3031–6.
- [59] Couzinie JP, Decamps B, Priester L. Interaction of dissociated lattice dislocations with a sigma 3 grain boundary in copper. *Int J Plast* 2005;21:759.
- [60] Christian JW, Mahajan S. Deformation twinning. *Prog Mater Sci* 1995;39:1–157.
- [61] Mughrabi H. Cyclic slip irreversibility and fatigue life: a microstructure-based analysis. *Acta Mater* 2013;61:1197.
- [62] Pippin R. Dislocation emission and fatigue crack growth threshold. *Acta Metall Mater* 1991;39:255–62.
- [63] Pippin R. The condition for the cyclic plastic deformation of the crack tip: the influence of dislocation obstacles. *Int J Fract* 1992;58:305–18.
- [64] Shyam A, Milligan WW. A model for slip irreversibility and its effect on the fatigue crack propagation threshold in a nickel-base superalloy. *Acta Mater* 2005;53:835–44.
- [65] Mughrabi H. Cyclic slip irreversibilities and the evolution of fatigue damage. *Metal Mater Trans B* 2009;40:431–53.
- [66] Weidner A, Sauzay M, Skrotzki W. Experimental evaluation of the cyclic slip irreversibility factor. *Key Eng Mater* 2011;465:223–6.
- [67] Differt K, Essmann U, Mughrabi H. A model of extrusions and intrusions in fatigued metals II. Surface roughening by random irreversible slip. *Philos Mag A* 1986;54:237–58.
- [68] Forsyth PJE. Fatigue damage and crack growth in aluminium alloys. *Acta Metall* 1963;11:703–15.
- [69] Mompou Fdr, Caillard D, Legros M, Mughrabi HI. In situ TEM observations of reverse dislocation motion upon unloading in tensile-deformed UFG aluminium. *Acta Mater* 2012;60:3402–14.
- [70] Lu G, Kiousis N, Bulatov VV, Kaxiras E. The Peierls–Nabarro model revisited. *Philos Mag Lett* 2000;80:675–82.
- [71] Escaig B. Cross-slipping process in the fcc structure. *J Phys* 1968;29:225.